ELSEVIER

J. Non-Newtonian Fluid Mech. 109 (2003) 93–114

Journal of Non-Newtonian Fluid Mechanics

www.elsevier.com/locate/jnnfm

The time-dependent, compressible Poiseuille and extrudate-swell flows of a Carreau fluid with slip at the wall

Georgios C. Georgiou*

Department of Mathematics and Statistics, University of Cyprus, P.O. Box 20537, 1678 Nicosia, Cyprus

Received 27 August 2002; received in revised form 10 October 2002; accepted 21 October 2002

Abstract

We solve the time-dependent, compressible Poiseuille and extrudate-swell flows of a shear-thinning fluid that obeys the Carreau constitutive model, using finite elements in space and a fully-implicit scheme in time. Slip is assumed to occur along the die wall following a non-monotonic slip equation that relates the wall shear stress to the slip velocity and is based on experimental measurements with polyethylene melts. Thus, the resulting flow curve is also non-monotonic, and consists of two stable positive-slope branches and a linearly unstable negative-slope branch. The steady-state numerical results compare well with certain analytical solutions for Poiseuille flow. The time-dependent calculations at fixed volumetric flow rates demonstrate the existence of periodic solutions in the unstable regime, due to the combination of compressibility and slip. Self-sustained oscillations of the pressure-drop and of the mass-flow rate are obtained. In the extrudate region, high-frequency, small amplitude waves are generated on the free-surface, which also oscillates radially. The wavelength and the amplitude of the free-surface waves and the amplitude of the oscillations in the radial direction are reduced, as the Reynolds number is decreased and approaches the conditions of the experiments.
© 2002 Elsevier Science B.V. All rights reserved.

Keywords: Poiseuille flow; Extrudate-swell flow; Carreau model; Compressibility; Slip; Stability

1. Introduction

Slip at the wall is considered to be a key factor in polymer extrusion instabilities, such as the stick–slip instability. A recent review article discussing wall slip and extrusion instabilities is provided by Denn [1]. Recent work concerning numerical modeling of polymer extrusion instabilities observed beyond the sharkskin regime, i.e. the stick–slip and gross-melt-fracture instabilities, has been reviewed by Achilleos et al. [2] who discuss three different mechanisms of instability: (a) combination of nonlinear slip with compressibility: (b) combination of non-linear slip with elasticity; and (c) constitutive instabilities. The

* Tel.: +357-2-2892208; fax: +357-2-2339061.
E-mail address: georgios@ucy.ac.cy (G.C. Georgiou).

0377-0257/02/$ – see front matter © 2002 Elsevier Science B.V. All rights reserved.
PII: S0377-0257(02)00164-7

objective of the present work is to investigate further the compressibility–slip instability by means of numerical simulations.

The compressibility–slip mechanism has been tested by Georgiou and Crochet [3] in the Newtonian case, with the use of an arbitrary non-monotonic slip equation relating the wall shear stress to the slip velocity. These authors numerically solved the time-dependent compressible Newtonian Poiseuille flow with non-linear slip at the wall, showing that steady-state solutions in the negative-slope regime of the flow curve (i.e. the plot of the wall shear stress versus the apparent shear-rate or the plot of the pressure-drop versus the volumetric flow rate) are unstable, in agreement with linear stability analysis. Self-sustained oscillations of the pressure-drop and of the mass-flow rate at the exit are obtained, when an unstable steady-state solution is perturbed, while the volumetric flow rate at the inlet is kept constant. These oscillations are similar to those observed experimentally with the stick–slip extrusion instability. Georgiou and Crochet [4] extended their calculations to the extrudate-swell problem to obtain oscillations of the free-surface in the unstable regime. The amplitude and the wavelength of the free-surface waves increase with compressibility.

In the present work, we proceed to more realistic numerical simulations of a shear-thinning fluid with an empirical slip equation that is based on the experimental measurements of Hatzikiriakos and Dealy [5,6] with a HDPE melt. We solve the time-dependent, compressible, axisymmetric Poiseuille and extrudate-swell flows of a Carreau fluid with slip at the wall, using finite elements in space and finite differences in time.

In Section 2, the governing equations and the slip equation are discussed. In Section 3, we present the analytical solutions for the steady, incompressible Poiseuille flow with slip at the wall and for the time-dependent, compressible Poiseuille flow with no-slip. The boundary and initial conditions and the numerical method are briefly discussed in Sections 4 and 5, respectively. In Section 6, we present and discuss both steady state and time-dependent numerical results. Finally, in Section 7, we summarize the conclusions.

2. Governing equations

The geometries of the axisymmetric Poiseuille and extrudate-swell flows are shown in Fig. 1. Letting p, $\boldsymbol{v}$, and $\boldsymbol{\sigma}$ denote the pressure, the velocity vector, and the stress tensor, respectively, the continuity and the momentum equations for time-dependent, compressible, isothermal viscous flow in the absence of body forces are as follows:

$$\frac{\partial \rho}{\partial t} + \nabla \cdot \rho \boldsymbol{v} = 0, \tag{1}$$

$$\rho \left(\frac{\partial \boldsymbol{v}}{\partial t} + \boldsymbol{v} \cdot \nabla \boldsymbol{v} \right) = \nabla \cdot \boldsymbol{\sigma}, \tag{2}$$

where ρ is the density. For compressible, generalized Newtonian flow with the bulk viscosity neglected, the stress tensor is written as

$$\boldsymbol{\sigma} = -p(\rho)\boldsymbol{I} + \eta(\mathrm{II}_{\boldsymbol{d}})(2\boldsymbol{d} - \tfrac{2}{3}\boldsymbol{I}\nabla \cdot \boldsymbol{v}), \tag{3}$$

where $\boldsymbol{I}$ is the unit tensor, $\boldsymbol{d}$ the rate-of-deformation tensor, defined as

$$\boldsymbol{d} = \tfrac{1}{2}[(\nabla \boldsymbol{v}) + (\nabla \boldsymbol{v})^{\mathrm{T}}], \tag{4}$$

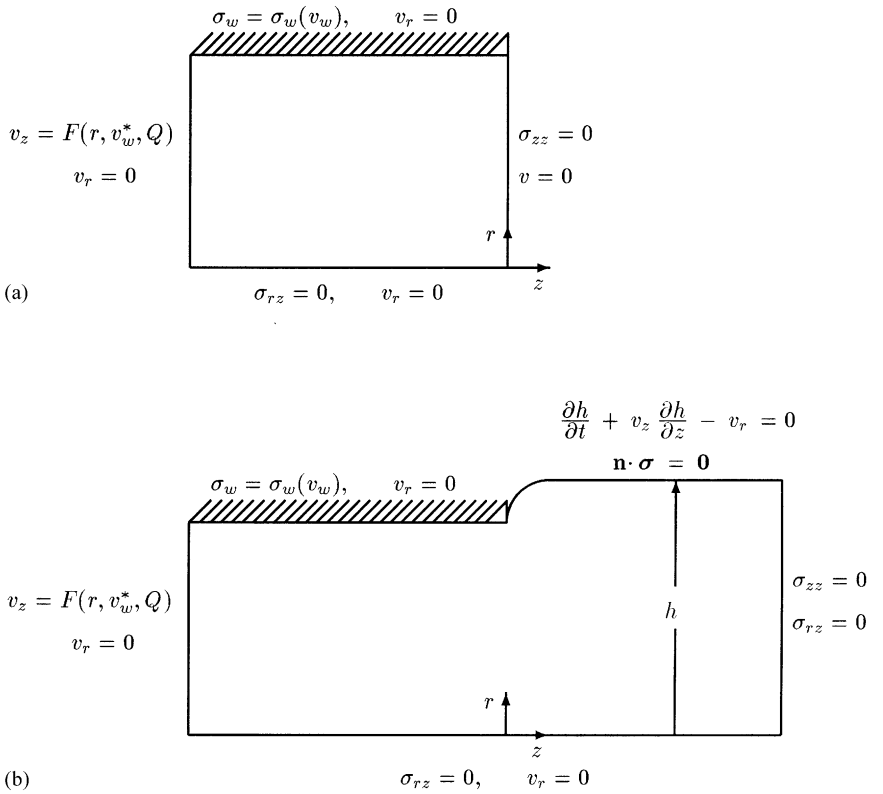

Fig. 1. Boundary conditions for the time-dependent, compressible, axisymmetric Poiseuille (a) and extrudate-swell (b) flows of a Carreau fluid with slip at the wall.

where η is the viscosity which is a function of the second invariant, $\mathrm{II}_{\boldsymbol{d}}$, of $\boldsymbol{d}$, and the superscript T denotes the transpose. Based on the excellent superposition of the data obtained from capillaries of various length-to-diameter ratios, Hatzikiriakos and Dealy [5] concluded that the pressure had a small effect on the viscosity of the HDPE melt used. The pressure dependence of the viscosity is thus neglected in this work.

For a power-law fluid,

$$\eta = K(2\mathrm{II}_{\boldsymbol{d}})^{n-1}, \tag{5}$$

where K is the consistency index, and n the power-law constant. An important limitation of the above model is the prediction of infinite zero-shear-rate viscosity. This results in severe convergence difficulties in regions of the flow field where $\mathrm{II}_{\boldsymbol{d}}$ is very small. (These include regions that are generally easy to solve, such as regions of uniform flow.) This problem is avoided by using the Carreau model which generalizes the power-law model as follows:

$$\eta = \eta_\infty + (\eta_0 - \eta_\infty)[1 + \lambda^2(2\mathrm{II}_{\boldsymbol{d}})^2]^{(n-1)/2}, \tag{6}$$

where η_0 is the zero-shear-rate viscosity, η_∞ the infinite-shear-rate viscosity, and λ is a time constant for which we have $\eta_0\lambda^{n-1} = K$. In this work, we use the values $n = 0.44$ and $K = 0.0178\,\mathrm{MPa\,s}^n$, provided by Hatzikiriakos and Dealy (resin A at 180 °C) [6]. We also assume that $\eta_0 = 0.03\,\mathrm{MPa\,s}$ and $\eta_\infty = 0$.

The above equations are completed by an equation of state relating the pressure to the density. We use the first-order expansion:

$$\rho = \rho_0[1 + \beta(p - p_0)], \tag{7}$$

where β is the isothermal compressibility, and ρ_0 the density at the reference pressure p_0. Hatzikiriakos and Dealy [6] provide the value $\beta = 9.923 \times 10^{-4}\,(\text{MPa})^{-1}$.

2.1. The slip equation

We use the following three-branch multi-valued slip model

$$v_w = \begin{cases} a_1\sigma_w^{m_1}, & 0 \le v_w \le v_{c2} \\ a_3\sigma_w^{m_3}, & v_{c2} \le v_w \le v_{min} \\ a_2\sigma_w^{m_2}, & v_w \ge v_{min} \end{cases} \tag{8}$$

where v_w is the relative velocity of the fluid with respect to the wall, σ_w the shear stress on the wall, v_{c2} the maximum slip velocity at σ_{c2}, and v_{min} is the minimum slip velocity at σ_{min}. The third branch is the power-law slip equation suggested by Hatzikiriakos and Dealy [6] for the right branch of their flow curve. The first branch results from the slip equation they propose for the left branch of their slope curve after substituting all parameters for resin A at 180 °C and taking the normal stress as infinite. (Taking the normal stress equal to zero results in a slip curve which almost overlaps with the third branch.) Finally, the second negative-slope branch, which corresponds to the unstable region of the flow curve for which no measurements have been possible, is just the line connecting the other two branches. Thus,

$$m_3 = \frac{\ln(v_{c2}/v_{min})}{\ln(\sigma_{c2}/\sigma_{min})} \quad \text{and} \quad a_3 = \frac{v_{c2}}{\sigma_{c2}^{m_3}}.$$

The values of all the slip equation parameters are shown in Table 1. A plot of the slip Eq. (8) is shown in Fig. 2.

Table 1
Values of the slip model parameters

Parameter	Value
a_1 ((MPa)$^{-m_1}$ cm/s)	125.09
m_1	3.23
a_2 ((MPa)$^{-m_2}$ cm/s)	1000
m_2	2.86
a_3 ((MPa)$^{-m_3}$ cm/s)	5.484×10^{-3}
m_3	−4.434
σ_{c2} (MPa)	0.27
σ_{min} (MPa)	0.19
v_{c2} (cm/s)	1.82
v_{min} (cm/s)	8.65

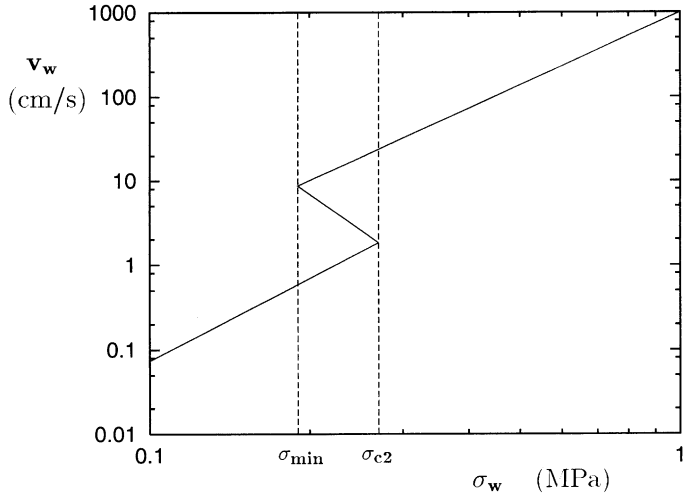

Fig. 2. The non-monotonic slip law based on the experimental data of Hatzikiriakos and Dealy for a high density polyethylene melt [5,6].

2.2. Non-dimensionalization

To non-dimensionalize the governing equations, we scale the lengths by the radius R, the velocity by the mean velocity V in the capillary, the pressure and the stress components by $\eta_0\lambda^{n-1}V^n/R^n$, the density by ρ_0, and the time by R/V. With this scaling, the continuity and momentum equations become

$$\frac{\partial\rho}{\partial t} + \nabla\cdot\rho\boldsymbol{v} = 0, \tag{9}$$

and

$$Re\,\rho\left(\frac{\partial\boldsymbol{v}}{\partial t} + \boldsymbol{v}\cdot\nabla v\right) = \nabla\cdot\boldsymbol{\sigma}, \tag{10}$$

where all variables are now dimensionless, and Re is the Reynolds number defined as

$$Re \equiv \frac{\rho_0 R^n V^{2-n}\lambda^{1-n}}{\eta_0}. \tag{11}$$

The dimensionless form of the stress tensor for a Carreau fluid is

$$\boldsymbol{\sigma} = -p\boldsymbol{I} + [1 + \Lambda^2(2\mathrm{II}_{\boldsymbol{d}})^2]^{(n-1)/2}(2\boldsymbol{d} - \tfrac{2}{3}\boldsymbol{I}\nabla\cdot\boldsymbol{v}), \tag{12}$$

where

$$\Lambda \equiv \frac{\lambda V}{R}. \tag{13}$$

The equation of state also becomes

$$\rho = 1 + Bp, \tag{14}$$

Table 2
Typical values of the dimensionless numbers

Dimensionless number	Value
n	0.44
Λ	349.2
m_1	3.23
A_1	0.0583
m_2	2.86
A_2	0.929
m_3	−4.43
A_3	4.04
σ^*_{c2}	1.738
σ^*_{min}	1.223
Re	1.43×10^{-5}
B	1.54×10^{-4}

where B is the compressibility number,

$$B \equiv \frac{\beta \eta_0 V^n}{\lambda^{1-n} R^n}. \tag{15}$$

The dimensionless form of the slip equation is

$$v_w = \begin{cases} A_1 \sigma_w^{m_1}, & 0 \le v_w \le v_{c2} \\ A_3 \sigma_w^{m_3}, & v_{c2} \le v_w \le v_{min} \\ A_2 \sigma_w^{m_2}, & v_w \ge v_{min} \end{cases} \tag{16}$$

where

$$A_i \equiv \frac{a_i \eta_0^{m_i} V^{m_i n - 1}}{\lambda^{m_i(1-n)} R^{m_i n}}, \quad i = 1, 2, 3, \tag{17}$$

and the dimensionless values of v_{c2} and v_{min} correspond to

$$\sigma^*_{c2} \equiv \frac{\sigma_{c2} R^n \lambda^{1-n}}{\eta_0 V^n} \quad \text{and} \quad \sigma^*_{min} \equiv \frac{\sigma_{min} R^n \lambda^{1-n}}{\eta_0 V^n}, \tag{18}$$

respectively. It should be noted that the volumetric flow rate is scaled by $\pi R^2 V$. Typical values of the dimensional numbers are tabulated in Table 2. These have been calculated by taking the value $500\,s^{-1}$ for the apparent shear-rate $\dot{\gamma}$, which for $R = 3.81 \times 10^{-2}\,cm^2$ yields $V = R\dot{\gamma}/4 = 5.24\,cm/s$.

3. Analytical solutions for steady Poiseuille flow

3.1. Incompressible Poiseuille flow with slip

For the incompressible flow of a Carreau fluid with the slip law given by

$$\sigma_w = \sigma_w(v_w), \tag{19}$$

it is easily shown that the steady-state solution is given by

$$v_z(r) = v_w + \frac{n}{n+1}\left(-\frac{1}{2}\nabla P\right)^{1/n}(1 - r^{(1/n)+1}), \tag{20}$$

where ∇P is the pressure gradient satisfying

$$-\nabla P = 2\sigma_w(v_w). \tag{21}$$

The dimensionless volumetric flow rate is given by

$$Q = v_w + \frac{n}{n+3}\left(-\frac{1}{2}\nabla P\right)^{1/n}. \tag{22}$$

3.2. Compressible Poiseuille flow with no-slip

The analytical solution of compressible Poiseuille flow of a Carreau fluid with no-slip at the wall can be obtained for $Re = 0$, with the assumption that the derivatives of the velocity across the die (i.e. in the r-direction) are much greater than in the direction of the flow (i.e. in the z-direction). The flow domain is defined by $-\infty < z \leq 0$ and $0 \leq r \leq 1$, and the pressure p is set to zero at $z = 0$. For a compressible fluid, the pressure gradient is a function of z and so is the volumetric flow rate. The mass-flow rate, $\dot{M}$, is, of course, constant. One finds that

$$p(z) = \frac{-1 + [1 - 2(n+1)((1/n)+3)^n B\dot{M}^n z]^{1/(n+1)}}{B} \tag{23}$$

and

$$v_z(r, z) = \frac{3n+1}{n+1}\frac{\dot{M}}{[1 - 2(n+1)((1/n)+3)^n B\dot{M}^n z]^{1/(n+1)}}(1 - r^{(1/n)+1}). \tag{24}$$

4. Boundary and initial conditions

The boundary conditions for the Poiseuille and extrudate-swell flows are shown in Fig. 1. Along the axis of symmetry, we have the usual symmetry conditions. Along the wall, the radial velocity is zero, whereas the axial velocity satisfies the slip Eq. (16). At the inlet plane, we assume that the radial velocity component, v_r, vanishes. In order to calculate the inlet condition for v_z, let us assume that the density is a weak function of r and that v_z, is of the following form:

$$v_z = (c_1 r^{(1/n)+1} + c_2 r + c_3)v_w^* + (c_4 r^{(1/n)+1} + c_5 r + c_6)Q,$$

where v_w^* is the unknown slip velocity at the inlet. The latter assumption is obviously true for the incompressible case. As shown in the previous section, it is also true for the compressible case, when inertia is neglected and the velocity gradients across the die are much greater than in the direction of the flow. For round Poiseuille flow, the velocity v_z at the inlet should satisfy the following conditions:

$$Q = \int_0^1 2v_z r\,\mathrm{d}r; \qquad \frac{\partial v_z}{\partial r} = 0 \quad \text{at} \quad r = 0; \qquad v_z = v_w^* \quad \text{at} \quad r = 1.$$

It turns out that

$$v_z = F(r, v_w^*, Q) = \frac{1}{n+1}[(3n+1)r^{(1/n)+1} - 2n]v_w^* + \frac{3n+1}{n+1}(1 - r^{(1/n)+1})Q. \tag{25}$$

The additional equation required for the calculation of the inlet velocity at the wall is provided by the fact that v_w^* satisfies the slip equation. It turns out that

$$\left(\frac{3n+1}{n}\right)^n (v_w^* - Q)^n = \sigma_w(v_w^*). \tag{26}$$

Provided that v_w, is a monotonic function of Q, one can easily calculate the velocity profile at the inlet for any value of Q.

In the case of Poiseuille flow, we assume that the radial velocity component vanishes at the outlet plane. The numerical results show that this assumption is reasonable at least for the relatively low compressibility numbers considered here. In the case of the extrudate-swell flow, we use the weaker condition $\sigma_{rz} = 0$. In both flows, the total normal stress is assumed to be zero, $\sigma_{zz} = 0$.

Finally, on the free-surface, we assume that surface tension is zero and impose vanishing normal and tangential stresses. Additionally, the unknown position $h(z, t)$ of the free-surface satisfies the kinematic condition:

$$\frac{\partial h}{\partial t} + v_z \frac{\partial h}{\partial z} - v_r = 0. \tag{27}$$

4.1. Initial conditions

In the case of Poiseuille flow, we use as initial condition the steady-state solution corresponding to a given volumetric flow rate Q at the inlet that we perturb by $\Delta Q = 0.001Q$ at $t = 0$. In the case of the extrudate-swell flow, we start with the steady-state solution of the stick–slip flow (i.e. with flat free-surface) and release the free-surface at $t = 0$.

5. The numerical method

We use the finite element formulation for solving this free-surface flow problem. The unknown position of the free-surface is calculated simultaneously with the velocity and pressure fields (full-Newton method). Furthermore, the density is eliminated by means of the equation of state (14). We use the standard biquadratic–velocity (P^2–C^0) and bilinear–pressure (P^1–C^0) elements with a quadratic representation for the position h of the free-surface. For the spatial discretization of the problem, we use the Galerkin forms of the continuity, momentum and kinematic equations. For the time discretization, we use the standard fully-implicit (Euler backward-difference) scheme.

6. Numerical simulations

The length L_1 of the capillary was taken to be equal to 20 (as in the experiments of Hatzikiriakos and Dealy [6]). For the extrudate region, we considered two different lengths, $L_2 = 5$ and 20, depending on

the wavelength of the free-surface oscillations. The finite element meshes were refined near the wall and the exit of the capillary. The mesh with $L_2 = 5$ consisted of 243 × 13 elements. With the exception of *Re* and *B*, the values of the dimensionless parameters are those shown in Table 2.

6.1. *Steady-state simulations*

To check the validity of the boundary condition at the inlet, we compared the numerical results with the analytical solution for steady, incompressible Poiseuille flow with slip at the wall, which is given in Section 3. As shown in Fig. 3a, the flow curve for $Re = B = 0$ is non-monotonic due to the form of the slip equation. Results have been obtained for different values of the volumetric flow rate; in all cases, the calculated velocity profiles coincide with the analytical solution. Such profiles are shown in Fig. 3b. An interesting observation is that, as the volumetric flow rate is increased, the velocity profile becomes rather plug. This agrees with experimental observations in the stick–slip and gross-melt-fracture regimes [2].

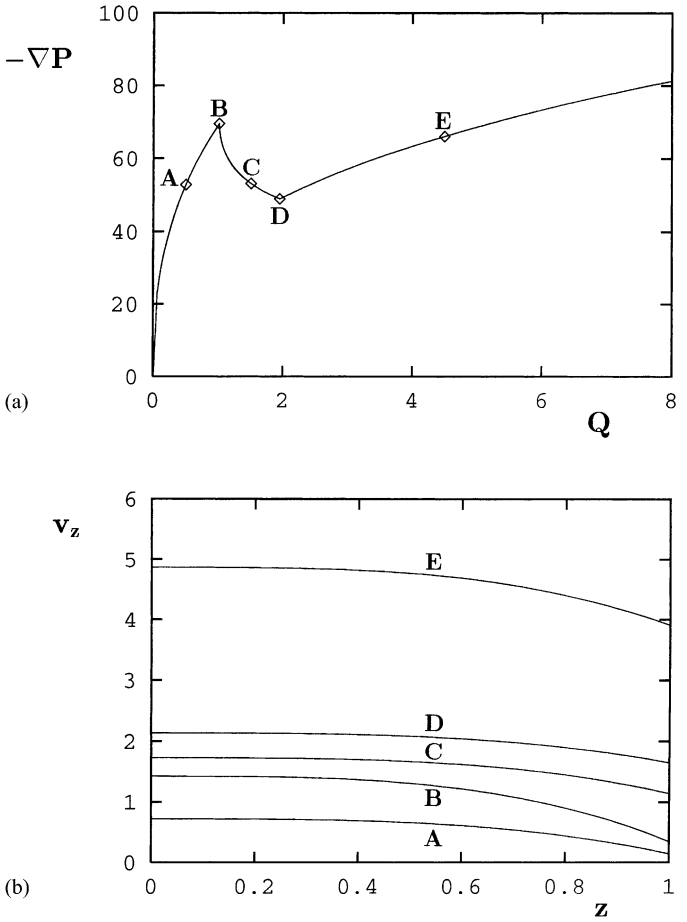

Fig. 3. (a) Flow curve for incompressible flow with slip at the wall; (b) velocity profiles at the indicated points of the flow curve; $Re = B = 0$, $n = 0.44$.

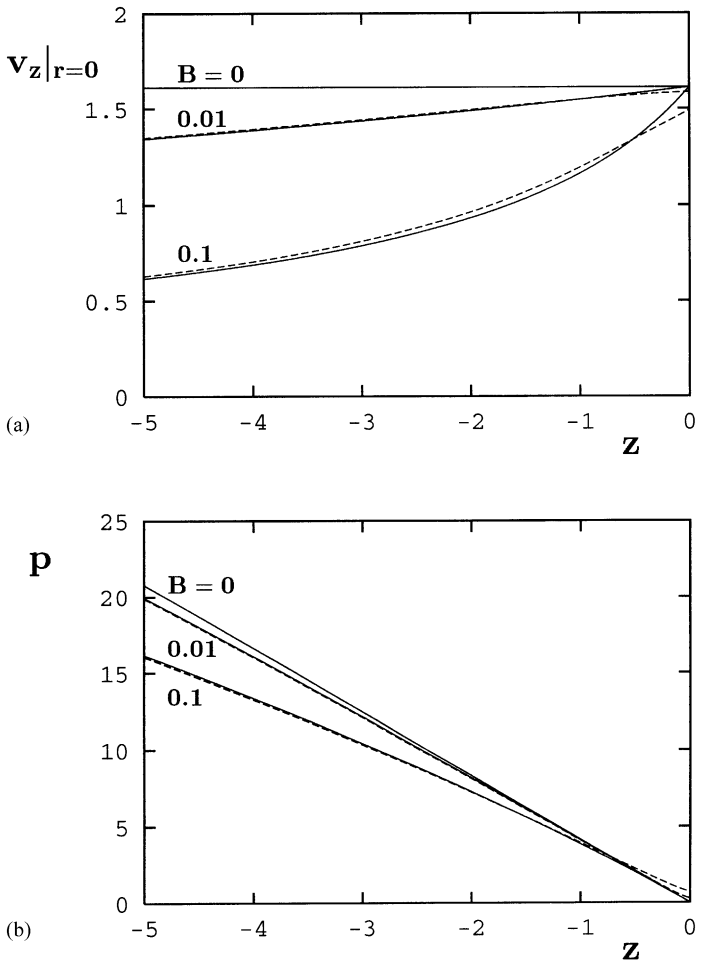

Fig. 4. Analytical (solid lines) vs. numerical (broken lines) steady-state results along the centerline for compressible flow with no-slip at the wall: (a) axial velocity; (b) pressure; $Re = 0$, $n = 0.44$, $\dot{M} = 1$.

Comparisons with the analytical solution in the case of steady, compressible Poiseuille flow without slip are shown in Fig. 4, for different values of the compressibility number B, $Re = 0$ and $\dot{M} = 1$. The axial velocity and the pressure along the centerline are plotted in Fig. 4a and b, respectively. Some discrepancies are observed near the exit but only at very high values of B, due to the outflow boundary condition. However, these high values of B correspond to markedly compressible flow; in the case of $B = 0.1$, density doubles in less than five radii upstream the exit, which is unrealistic. The runs for this extreme case were just used as a check to the numerical scheme and the assumptions we have made. Note that the pressure-drop is reduced as compressibility increases.

In Fig. 5, we show the (steady state) flow curves corresponding to both slip and no-slip with $Re = 1.43 \times 10^{-5}$ and $B = 1.54 \times 10^{-4}$. Due to the small values of Re and B, the flow curve is practically the same as that for $Re = B = 0$ (Fig. 3). The reduction of the pressure-drop due to slip is appreciable at higher volumetric flow rates, especially beyond the left positive-slope branch. Here, $-\nabla P$ is the pressure-drop

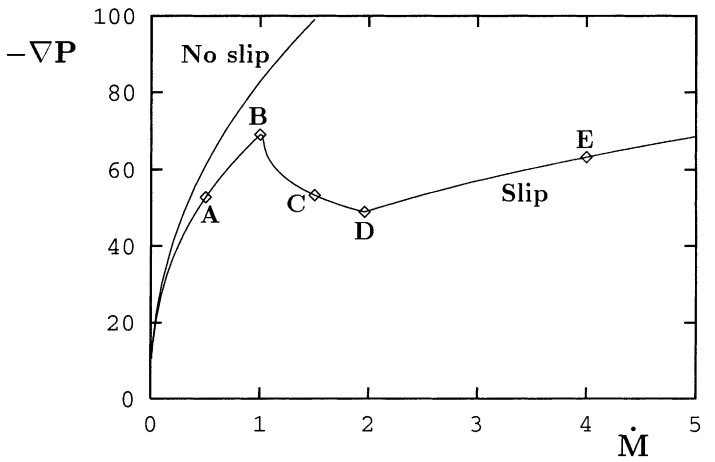

Fig. 5. Flow curves for $Re = 1.43 \times 10^{-5}$ and $B = 1.54 \times 10^{-4}$.

along the wall (the pressure-drop along the plane of symmetry is slightly lower). Since the volumetric flow rate, Q, is not constant in the direction of the flow, $-\nabla P$ is plotted versus the mass-flow rate $\dot{M}$. It should be noted, however, that $\dot{M} = Q$ at the exit.

A consequence of slip, known from both experiments [7] and simulations [4], is the reduction of the swelling. This reduction is enhanced as the volumetric flow rate is increased, as illustrated in Fig. 6, where we plot the steady free-surface profiles calculated for five different values of the volumetric flow rate, corresponding to the various regimes of the flow curve. (These points are indicated on the flow curve of Fig. 5.) A slight swelling reduction is also observed in the no-slip case. This is due to the increase of the actual Reynolds number [8].

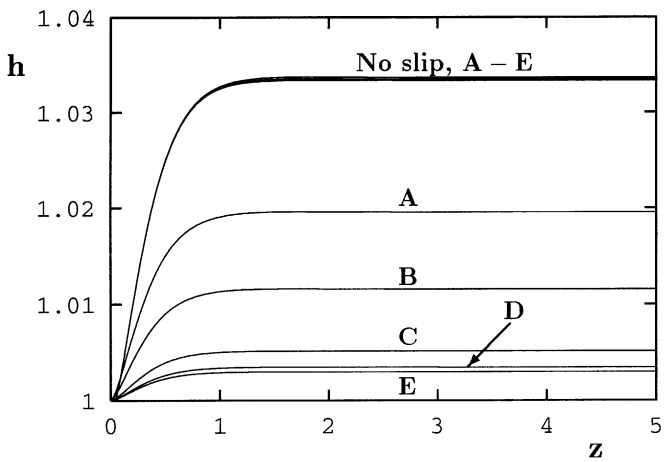

Fig. 6. Free-surface profiles for the five volumetric flow rates (0.5, 1.0, 1.5, 1.96, 4.0) indicated in Fig. 6; $Re = 1.43 \times 10^{-5}$, $B = 1.54 \times 10^{-4}$.

6.2. Time-dependent simulations

As already mentioned, steady-state Poiseuille flow solutions are perturbed by slightly changing the value of the corresponding flow rate Q to $1.001Q$. Different possibilities have been examined and the main conclusions can be summarized as follows.

(a) If the flow is incompressible and no-slip is applied along the wall, the steady-state solution corresponding to the new volumetric flow rate is instantaneously obtained.
(b) If the flow is incompressible and slip is present, the time-dependent solution moves gradually to the new steady state without the appearance of any oscillations, even when the imposed volumetric flow rate is in the negative-slope regime.
(c) If the flow is compressible and no-slip occurs at the wall, the solution moves to the new steady state without any oscillations.
(d) If the flow is compressible and slip is present, the behavior of the time-dependent solution depends on whether the new value of Q corresponds to a positive-slope branch or to the negative-slope branch which is unstable. In the first case, the new steady state is obtained without any oscillations, whereas, in the second case, the solution is oscillatory and, after a transition period, becomes periodic. All the results presented later have been obtained in the unstable regime.

We first obtained solutions for $Re = 0.1$, $B = 1.541 \times 10^{-4}$ and various values of Q. This value of the Re is purposely chosen to be much higher than the experimental one (1.43×10^{-5}), in order to enhance the oscillations. In Figs. 7–9, we visualize the solutions obtained with $Q = 1.1$, 1.5 and 1.9, by plotting the evolution of the pressure-drop, the evolution of the mass-flow rates at the inlet and the outlet, and the trajectory of the time-dependent solution on the flow curve plane. In all cases, self-sustained oscillations of the pressure-drop and the mass-flow rate are obtained after a transition period which becomes longer as one moves from the maximum to the minimum of the flow curve. These oscillations are similar to those observed experimentally in the stick–slip extrusion instability regime.

The establishment of the periodic solution is marked by the limit cycle reached on the flow-curve plane. Note that the pressure-drop oscillations are extended above the maximum and below the minimum of the steady-state flow curve, whereas the mass-flow-rate oscillations are extended to the left of the maximum and to the right of the minimum. As a result, the limit cycle does not follow any parts of the positive-slope branches of the flow curve, which is in disagreement with experimental observations [6,9]. This drawback is most probably due to the omission of the barrel from the simulations; it is also exhibited by the one-dimensional model of Greenberg and Demay [10], which does not include the barrel region. Note that most one-dimensional phenomenological relaxation/oscillation models require as input the experimental (steady state) flow curve. These models are based on the compressibility/slip mechanism and describe oscillations of the pressure and the volumetric flow rate in the stick–slip instability regime (see [11–13] and references therein).

The limit cycles in Figs. 7–9 illustrate some well-known characteristics of the stick–slip flow instability. Once pressure reaches its maximum, the volumetric flow rate increases rapidly to its maximum value (spurt). Then, pressure starts decreasing reaching its minimum value, and the volumetric flow rate decreases. Once the minimum of the volumetric flow rate is reached, pressure increases again, and the cycle repeats in a time-periodic manner. For $Q = 1.5$ and for Reynolds numbers ranging from 0.1 to 0.001, the maximum mass-flow rate was found to range from 9 to about 15 times the minimum value. Hatzikiriakos and Dealy [6] reported that with resin A at 160 °C the mass-flow rate

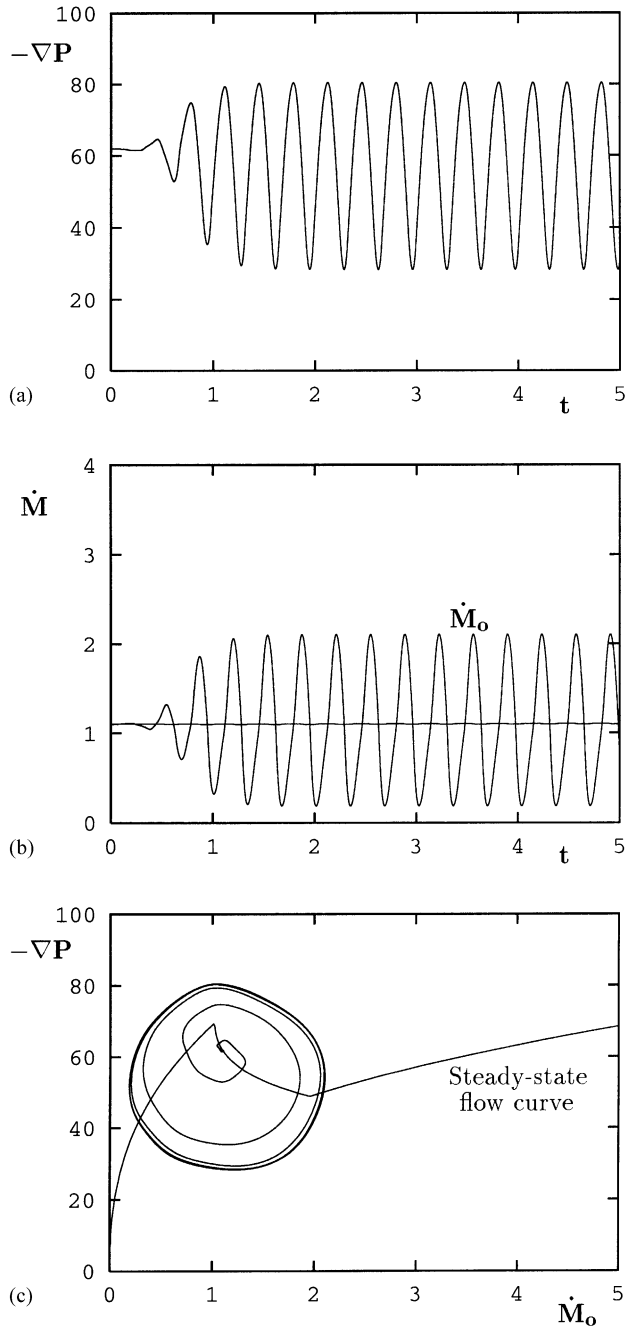

Fig. 7. Transient Poiseuille flow of a Carreau fluid with $n = 0.44$, $Re = 0.1$ and $B = 1.541 \times 10^{-4}$ when the steady state at $Q = 1.1$ is slightly perturbed: (a) pressure-drop; (b) mass-flow rates at the inlet and the outlet ($\dot{M}_o$); (c) trajectory of the solution on the flow curve plane.

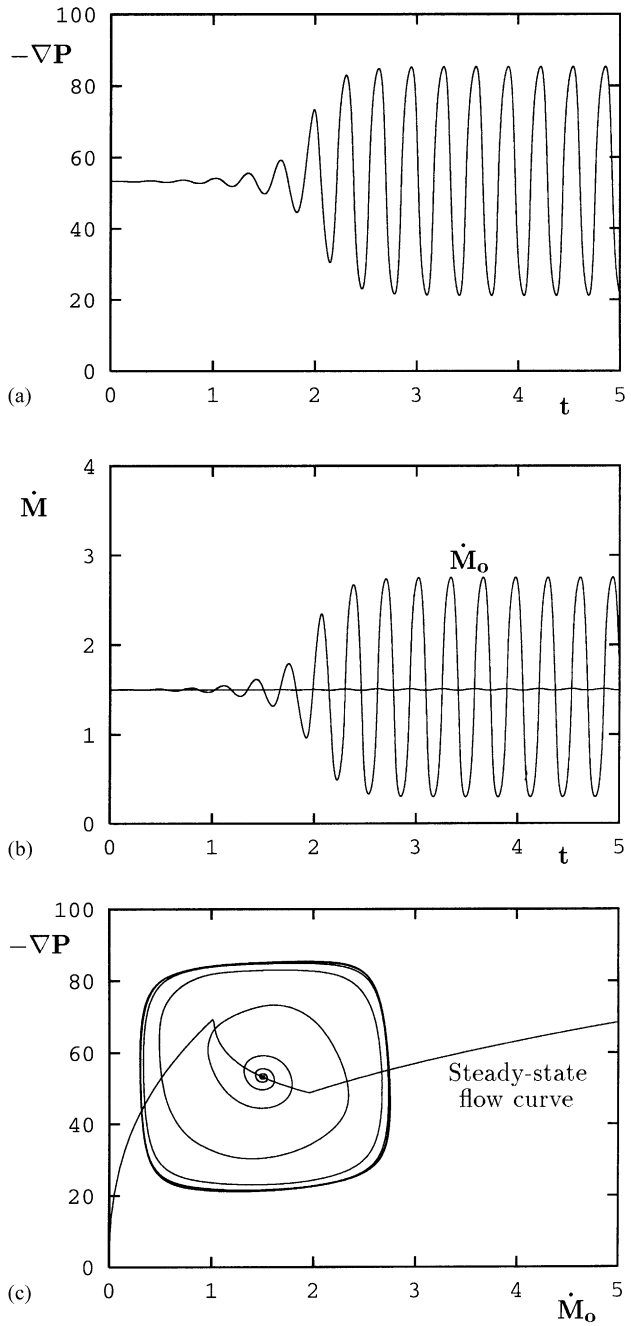

Fig. 8. Transient Poiseuille flow of a Carreau fluid with $n = 0.44$, $Re = 0.1$ and $B = 1.541 \times 10^{-4}$ when the steady state at $Q = 1.5$ is slightly perturbed: (a) pressure-drop; (b) mass-flow rates at the inlet and the outlet ($\dot{M}_o$); (c) trajectory of the solution on the flow curve plane.

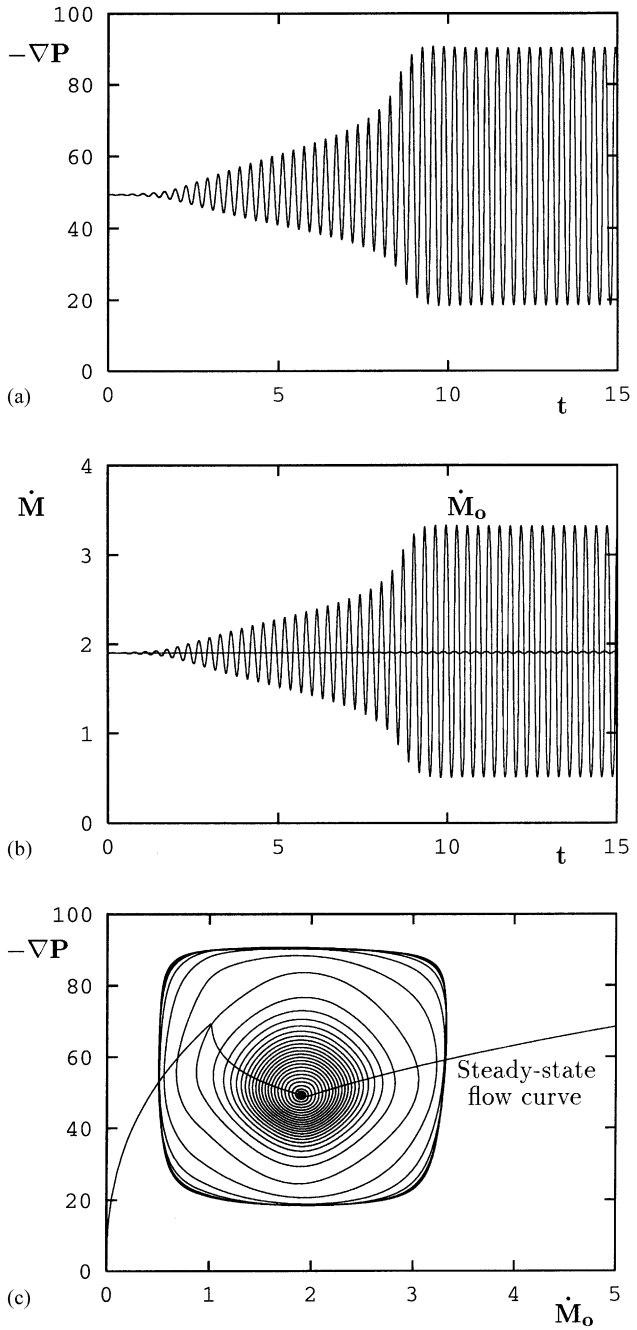

Fig. 9. Transient Poiseuille flow of a Carreau fluid with $n = 0.44$, $Re = 0.1$ and $B = 1.541 \times 10^{-4}$ when the steady state at $Q = 1.9$ is slightly perturbed: (a) pressure-drop; (b) mass-flow rates at the inlet and the outlet ($\dot{M}_o$); (c) trajectory of the solution on the flow curve plane.

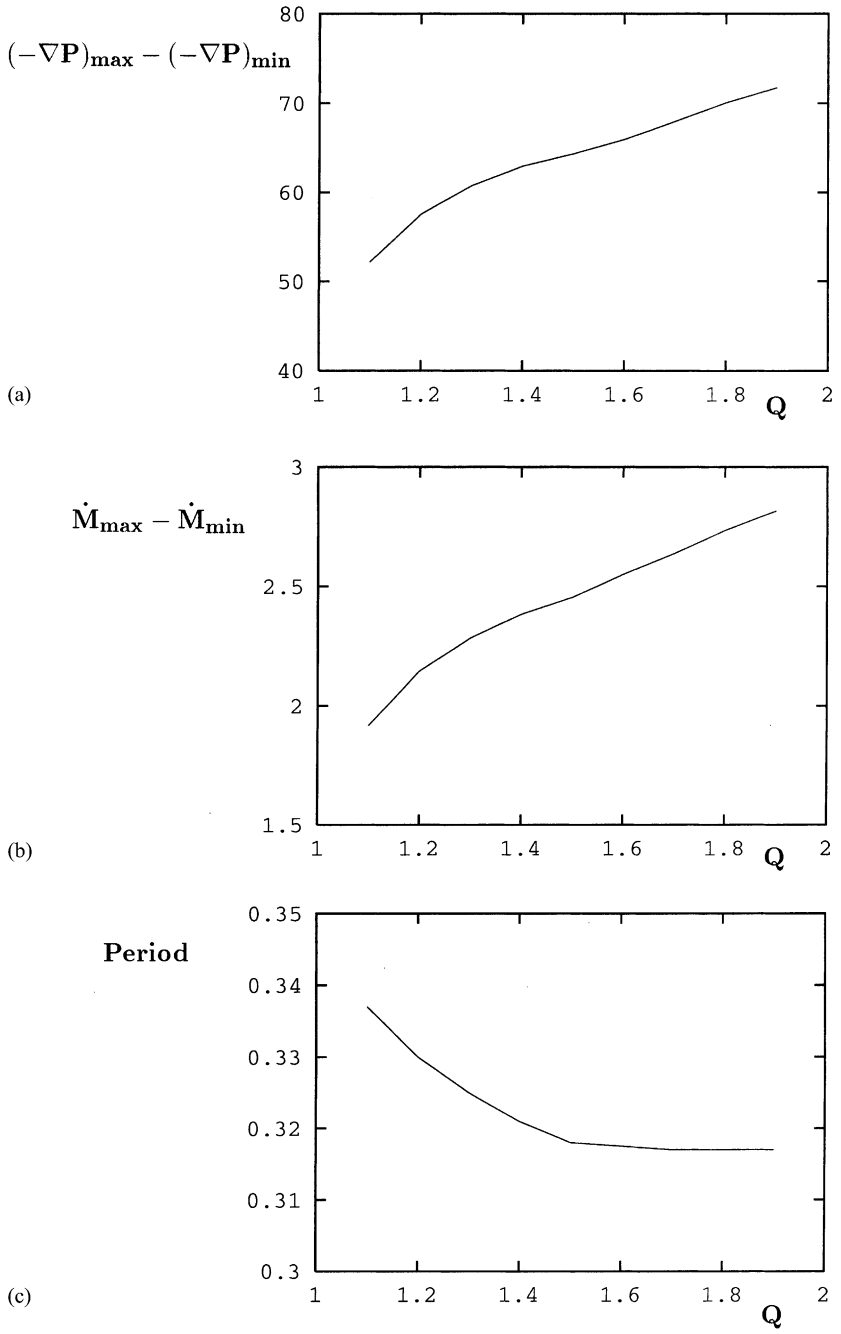

Fig. 10. Variations of the amplitude of the pressure-drop (a), mass-flow rate at the outlet (b), and the period (c) of the oscillations with Q; transient Poiseuille flow of a Carreau fluid with $n = 0.44$, $Re = 0.1$ and $B = 1.541 \times 10^{-4}$ with the steady state at Q slightly perturbed.

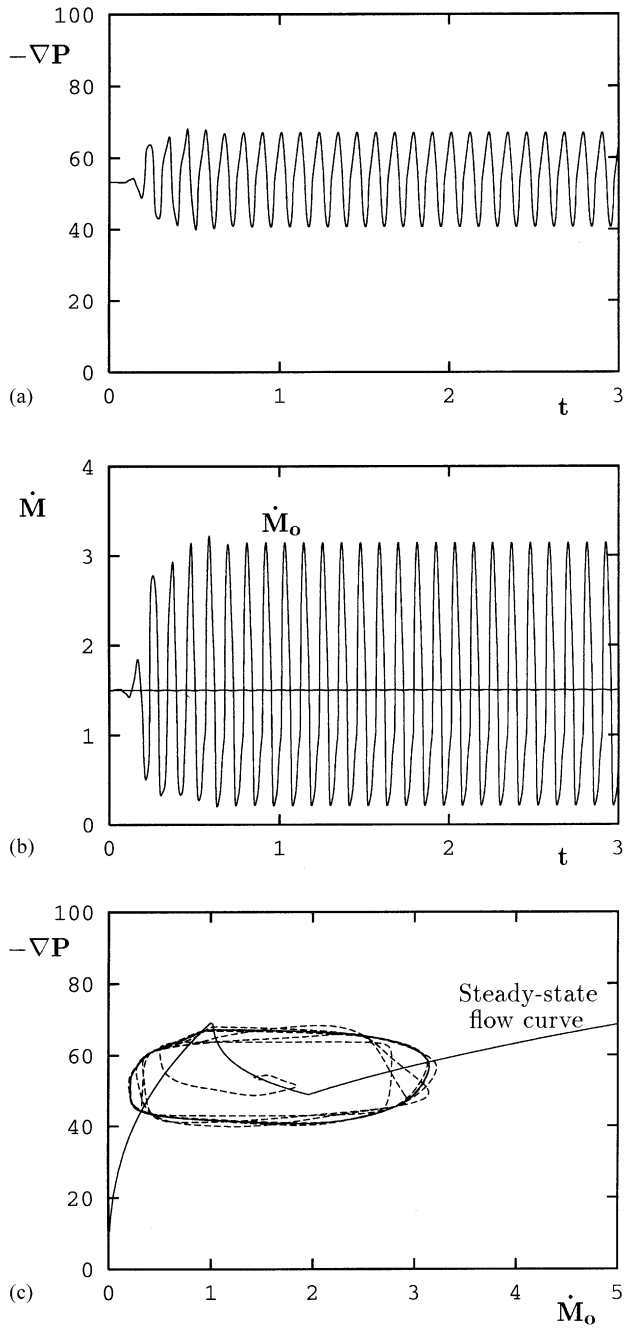

Fig. 11. Transient Poiseuille flow of a Carreau fluid with $n = 0.44$, $Re = 0.01$ and $B = 1.541 \times 10^{-4}$ when the steady state at $Q = 1.5$ is slightly perturbed: (a) pressure-drop; (b) mass-flow rates at the inlet and the outlet ($\dot{M}_o$); (c) trajectory of the solution on the flow curve plane.

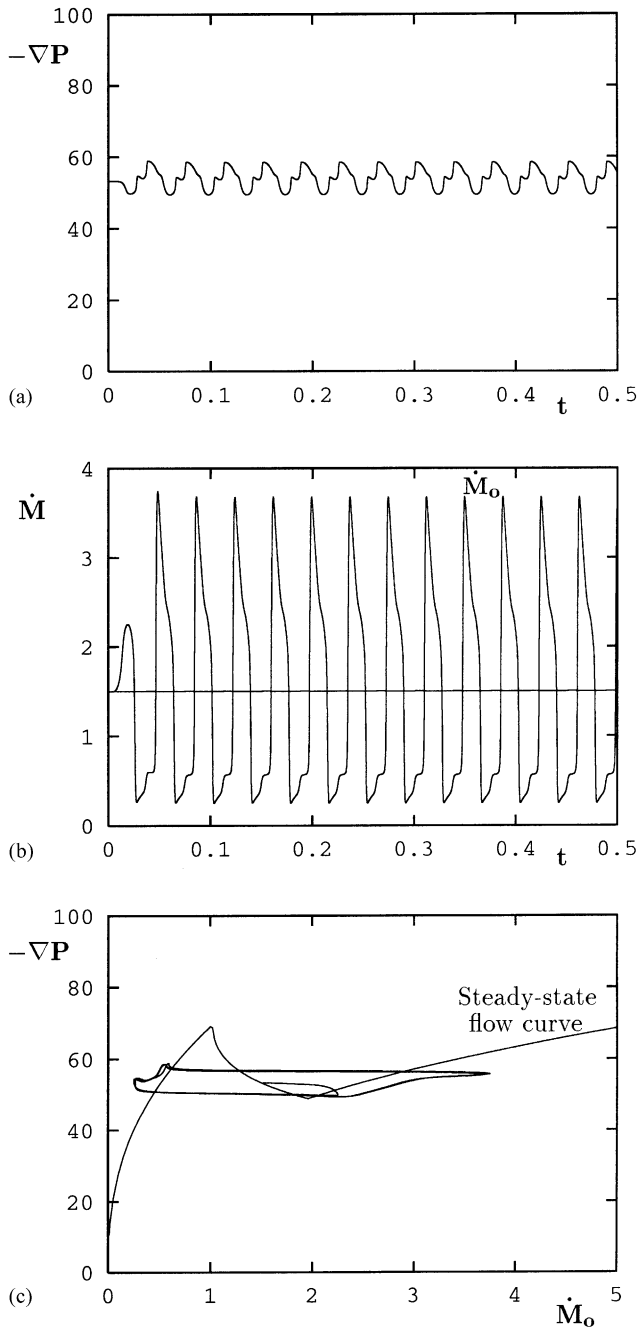

Fig. 12. Transient Poiseuille flow of a Carreau fluid with $n = 0.44$, $Re = 0.001$ and $B = 1.541 \times 10^{-4}$ when the steady state at $Q = 1.5$ is slightly perturbed: (a) pressure-drop; (b) mass-flow rates at the inlet and the outlet ($\dot{M}_o$); (c) trajectory of the solution on the flow curve plane.

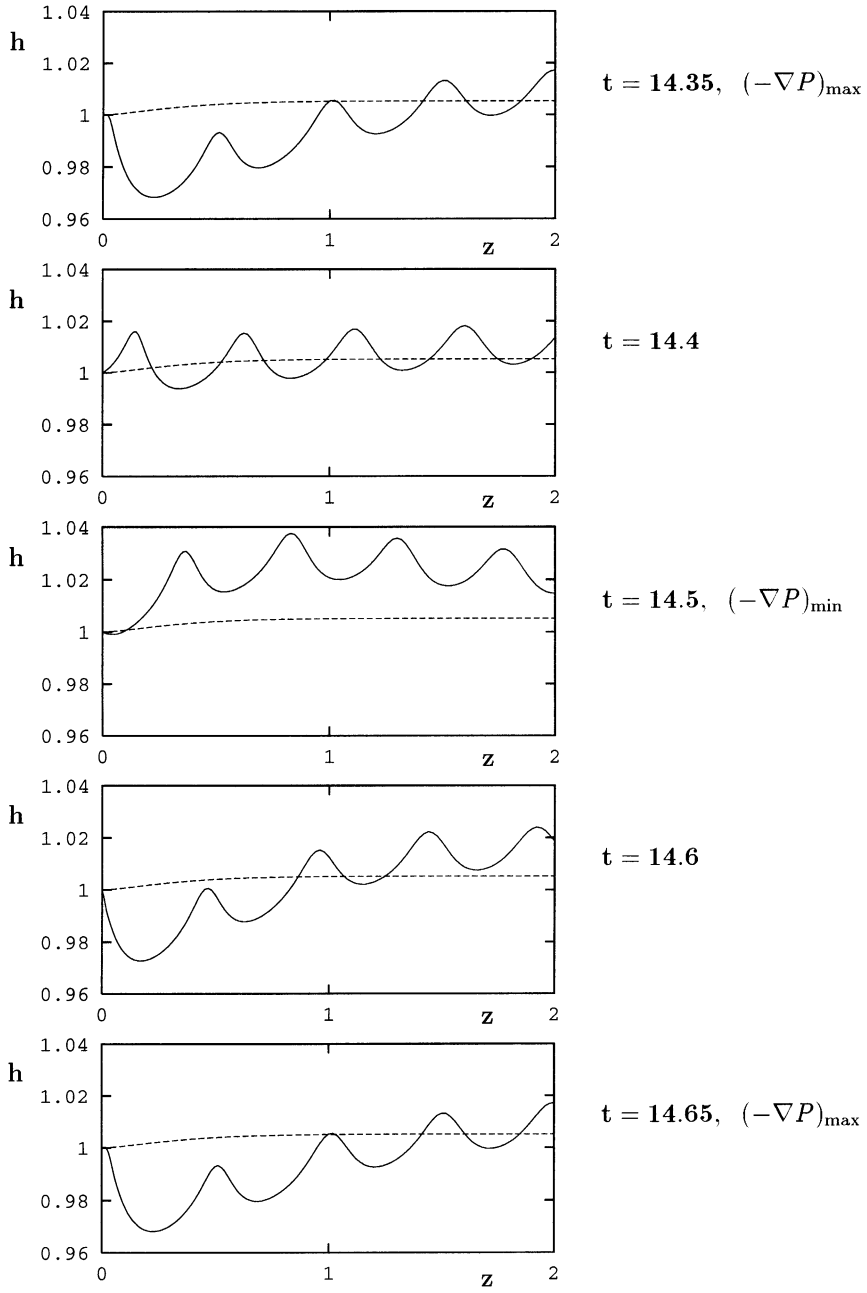

Fig. 13. Evolution of the free-surface during a cycle after the periodic solution is established. The broken line shows the unstable steady-state position of the free-surface; $n = 0.44$, $Re = 0.1$, $B = 1.541 \times 10^{-4}$ and $Q = 1.5$.

suddenly increases by a factor of about 8. Given that the material parameters we used correspond to a higher temperature (180 °C) and the minimum value depends on the shape of the negative-slope branch of the slip equation, the agreement of the numerical results with the experiments is quite satisfactory.

As illustrated in Fig. 10, both the amplitude and the frequency of the oscillations increase with Q. The increase in the amplitude of both the pressure-drop and the mass-flow-rate oscillations is also deduced from the increasing size of the limit, cycles in Figs. 7–9. The results in Figs. 7–10 show that the amplitude and the frequency of the oscillations depend on the shape of the flow curve, which, in turn, is intrinsically linked to the form of the slip equation, especially in the unstable negative-slope regime. As already mentioned, due to the lack of experimental data in this regime, our slip equation has been constructed by connecting with a straight line the two positive-slope branches of the experimental slip curves, which evidently poses a severe limitation on our simulations.

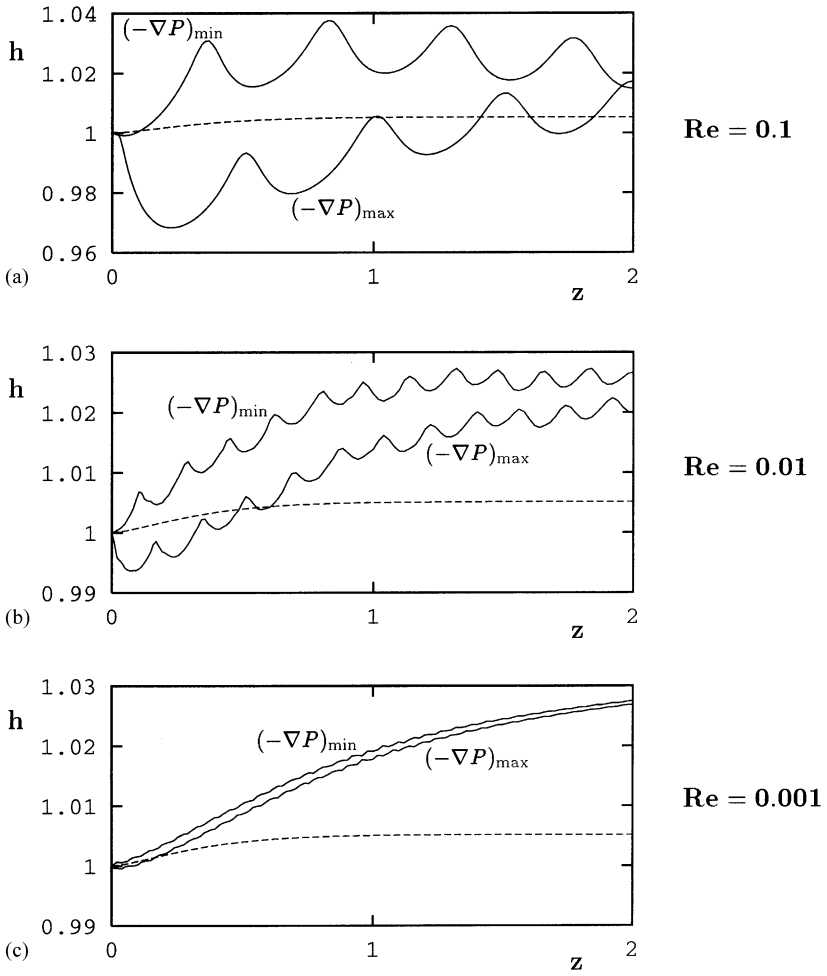

Fig. 14. Representative free-surface waves for different Reynolds numbers (a–c). The broken line shows the unstable steady-state position of the free-surface: $n = 0.44$, $B = 1.541 \times 10^{-4}$ and $Q = 1.5$.

To study the effect of *Re* for $Q = 1.5$, we obtained solutions for $Re = 0.01$ and 0.001, which are shown in Figs. 11 and 12, respectively. We observe that as the Reynolds number is reduced, the amplitude of the pressure-drop oscillations is reduced while that of the mass-flow-rate oscillations is increased. Moreover, the frequency of the oscillations is increased considerably. As a result, much smaller time-steps must be employed for these runs. This together with the expected very small amplitude of the pressure-drop oscillations prevent us from pursuing simulations for smaller values of the *Re*, such as the experimental value 1.43×10^{-5}.

The time-dependent simulations of the extrudate-swell flow were obtained by starting with the steady-state solution corresponding to a flat free-surface (stick–slip flow) and letting the free-surface move at $t = 0$. In the unstable regime, waves appear on the free-surface, in addition to the pressure-drop and mass-flow-rate oscillations. In Fig. 13, we show representative free-surface profiles obtained with $Re = 0.1$, $B = 1.541 \times 10^{-4}$ and $Q = 1.5$ during one complete cycle (from a pressure-drop maximum to the next one), after the periodic solution is established. In addition to the motion of the free-surface waves in the flow direction, the free-surface oscillates in the radial direction as well. Swelling is minimized at pressure-drop maxima. This result is in agreement with the experiments of Pérez González et al. [14], who worked with polyethylene melts and observed that severe contractions in the extrudate diameter occur at pressure maxima.

Finally, the effect of *Re* on the free-surface waves is illustrated in Fig. 14, where we show representative free-surface profiles obtained with $B = 1.541 \times 10^{-4}$, $Q = 1.5$ and $Re = 0.1$ with $L_2 = 20$, and $Re = 0.01$ and 0.001, with $L_2 = 5$. The amplitude and the wavelength of the free-surface waves and the amplitude of the oscillations in the radial direction are reduced as *Re* approaches zero. Another important observation is that swelling is enhanced by the oscillations, since the free-surface oscillates well above and not, about its unstable steady-state position. Due to the small size of the free-surface oscillations, no simulations have been attempted for smaller values of the Reynolds number.

7. Conclusions

We used finite elements to simulate the time-dependent, compressible Poiseuille and extrudate-swell flows of a Carreau fluid, assuming that slip occurs along the die wall following a non-monotone slip law that is based on the experimental findings of Hatzikiriakos and Dealy [5,6] for certain polyethylene melts. The steady-state numerical results compare well with the analytical solutions for incompressible Poiseuille flow with slip and for the compressible Poiseuille flow without slip, and predict the expected reduction of the swelling as slip is enhanced.

The time-dependent calculations at fixed volumetric flow rates in the unstable negative-slope regime of the flow curve demonstrate that combination of compressibility and slip results in periodic solutions, i.e. in self-sustained oscillations of the pressure-drop and of the mass-flow rate, as is the case with the stick–slip extrusion instability. The free-surface is characterized by high-frequency, small amplitude waves traveling in the flow direction and oscillates in the radial direction. The wavelength and the amplitude of the free-surface waves and the amplitude of the oscillations in the radial direction are reduced, as the Reynolds number goes to zero.

The limitations of the present work indicate directions for future research. The slip equation we employed may be based on experimental data but the added negative-slope branch is arbitrary. In addition, the slip equation is not dynamic nor it accounts for the effect of pressure on slip. Another limitation of the

present simulations comes form the axisymmetry assumption. The experimental data concern, in most cases, extrudates with asymmetric waves, i.e. the actual extrudate is three-dimensional. Finally, including the reservoir is necessary in order not only to account for the compression and decompression of most part of the fluid but also to account for the effect of upstream instabilities which is known to be crucial (see [2]). For example, experiments show that the period of the pressure-drop oscillations decreases as the volume of the melt in the reservoir increases [6,9,15]. With the large amount of the compressible melt in the reservoir region taken into account, numerical simulations will be possible at low Reynolds numbers corresponding to the experiments. Moreover, the inclusion of the reservoir region is necessary for obtaining limit cycles following the steady-state branches of the flow curve, i.e. for obtaining pressure and extrudate flow rate oscillations characterized by abrupt changes, as is the experiments. Only such abrupt changes can lead to extrudates with alternating relatively smooth and sharkskin regions, which is the basic characteristic of the stick–slip instability.

Acknowledgements

This research was partially supported by the Cyprus Foundation for the Promotion of Research (PENEK Program 02/2000).

References

[1] M.M. Denn, Extrusion instabilities and wall slip, Annu. Rev. Fluid Mech. 33 (2001) 265.
[2] E. Achilleos, G. Georgiou, S.G. Hatzikiriakos, On numerical simulations of polymer extrusion instabilities, Appl. Rheol. 12 (2002) 88.
[3] G.C. Georgiou, M.J. Crochet, Time-dependent compressible extrudate-swell problem with slip at the wall, J. Rheol. 38 (1994) 1745.
[4] G.C. Georgiou, M.J. Crochet, Compressible viscous flow in slits with slip at the wall, J. Rheol. 38 (1994) 639.
[5] S.G. Hatzikiriakos, J.M. Dealy, Wall slip of molten high density polyethylenes. II. Capillary rheometer studies, J. Rheol. 36 (1992) 703.
[6] S.G. Hatzikiriakos, J.M. Dealy, Role of slip and fracture in the oscillating flow of HDPE in a capillary, J. Rheol. 36 (1992) 845.
[7] A.M. Kraynik, W.R. Schowalter, Slip at the wall and extrudate roughness with aqueous solutions of polyvinyl alcohol and sodium borate, J. Rheol. 25 (1981) 95.
[8] G.C. Georgiou, T.C. Papanastasiou, J.O. Wilkes, Laminar jets at high Reynolds and high surface tension, AIChE J. 24 (1988) 1559.
[9] V. Durand, B. Vergnes, J.F. Agassant, E. Benoit, R.J. Koopmans, Experimental study and modeling of oscillating flow of high density polyethylenes, J. Rheol. 40 (1996) 383.
[10] J.M. Greenberg, Y. Demay, A simple model of the melt-fracture instability, Eur. J. Appl. Math. 5 (1994) 337.
[11] K.P. Adewale, A.I. Leonov, Modelling spurt and stress oscillations in flows of molten polymers, Rheol. Acta 36 (1997) 110.
[12] C.F.J. Den Doelder, R.J. Koopmans, J. Molenaar, A.A.F. Van de Ven, Comparing the wall slip and the constitutive approach for modelling spurt instabilities in polymer melt flows, J. Non-Newtonian Fluid Mech. 75 (1998) 25.
[13] M. Ranganathan, M.R. Mackley, P.H.J. Spitteler, The application of the multi-pass rheometer to time-dependent capillary flow measurements of a polyethylene melt, J. Rheol. 43 (1999) 443.
[14] J. Pérez González, L. Pérez-Trejo, L. de Vargas, O. Manero, Inlet instabilities in the capillary flow of polyethylene melts, Rheol. Acta 36 (1997) 677.
[15] E.E. Rosenbaum, S.G. Hatzikiriakos, C.W. Stewart, Flow implications in the processing of tetrafluoroethylene/hexafluoropropylene copolymers, Intern. Polym. Process. 3 (1995) 204.